

Thermopneumatic Pixels for Fast, Localized, Low-Voltage Touch Feedback

Max Linnander, Yon Visell *Member, IEEE*,

Abstract—We present thermopneumatic pixels (TPPs), which are tactile actuators designed for rapid fabrication and straightforward integration into compact wearable and surface-based haptic systems. Each TPP converts low-voltage (~ 10 V) electrical pulses into transient pressure increases within a sealed cavity, producing out-of-plane forces and displacements suitable for tactile stimulation. The architecture enables scalable fabrication and spatially distributed actuation while maintaining simple electrical interfacing. The TPPs are constructed from inexpensive, readily available materials using straightforward layer-based assembly, facilitating rapid prototyping and integration into interactive devices. Mechanical characterization demonstrates peak forces exceeding 1 N and millimeter displacements. We further present driving electronics for operating multiple TPP modules concurrently and report perceptual study results demonstrating the effectiveness of the resulting tactile feedback. Together, these results establish low-voltage thermopneumatic actuation as an accessible and high-performance approach for embedding tactile feedback into experimental and consumer-facing interfaces.

Index Terms—Haptics, Thermopneumatic, Actuator, Tactile, Pixels, Rapid prototyping, Human-computer interaction, Low-voltage

I. INTRODUCTION

Haptic interfaces have advanced rapidly, but compact systems that deliver strong, localized tactile cues are still challenging to realize in practice. In many cases the obstacle is less the availability of actuators and more the burden of implementation, requiring specialized fabrication, demanding drive electronics, and integration steps that are difficult to reproduce. Actuator platforms that are simple to fabricate and easy to integrate can make the technology more widely available, complementing recent community efforts toward usable haptic platforms and open-source tools [1]–[4].

To be broadly applicable across implementations and contact conditions, haptic actuators should span a useful envelope of mechanical outputs. Required force, displacement, and temporal bandwidth vary with anatomical site, contact area, and preload, and no single operating metric is universally appropriate [5]. A practical goal is therefore an actuator family that can be readily scaled or tuned to deliver forces on the order of 10^{-3} – 10^0 N, displacements of 10^{-6} – 10^{-3} m, and dynamics from milliseconds to seconds, consistent with regimes used across haptics [6], [7].

Many actuator technologies satisfy portions of this envelope, but practical implementation often exposes tradeoffs that limit replication and deployment in compact systems. Electromagnetic actuators remain widely available, yet as

dimensions shrink, they are increasingly limited by current density, heat generation, and the nontrivial magnetic and mechanical packaging [8]. Electrostatic and dielectric-elastomer approaches can achieve high bandwidth and large strain, but their kilovolt drive voltages complicate insulation, routing, and safe integration in compact systems and multi-element arrays [9]–[11]. Meanwhile, emerging soft actuation approaches—including electroactive polymers and electroosmotic devices—are promising yet frequently depend on specialized materials, fabrication workflows, or bespoke driving hardware that can limit accessibility and widespread implementation [12]–[14].

Thermal actuation offers a combination of accessibility and integrability: heaters and compliant structures can be realized with common materials and straightforward fabrication steps, and the resulting devices are often driven at modest voltages with minimal specialized electronics [12]. However, many thermally driven mechanisms are fundamentally constrained by thermal inertia. Much of the deposited energy raises the temperature of solid or liquid masses, and the associated time constants scale with thermal mass (volumetric heat capacities ~ 1 J/cm³K), leading to slow transients in the 10^0 – 10^2 s range [15], [16].

Thermopneumatic approaches offer the potential for faster responses by heating a captive gas to perform mechanical work. Gases have lower volumetric heat capacities than solids and liquids (~ 0.001 J/cm³K), offering the potential for rapid responses. Although such configurations have been studied, the heating element has often been integrated in the wall of the gas-filled cavity, yielding long response times and low forces due to heat loss to the walls [17], [18]. Photo-thermopneumatic actuators have circumvented this by depositing radiative heat onto a low-thermal-inertia absorber, suspended in the working gas cavity. This has enabled rapid transfer of heat into the gas, but requires additional optical components and losses due to the conversion of electrical into optical energy [19], [20]. These comparisons motivate our concept of suspending a thin resistive wire in a cavity encapsulating a captive gas.

Here, we present millimeter-scale thermopneumatic pixels (TPPs); haptic actuators implemented in mechanically flexible modules that can be used for wearable and surface-based haptics. Each TPP consists of a sealed cavity containing a suspended resistive wire that is electrically heated using low-voltage drive signals (~ 10 V). Due to its low thermal inertia, the wire rapidly heats, transferring energy to the encapsulated gas, which produces a transient increase in pressure that deflects an elastic membrane and generates out-of-plane force and displacement. This mechanism enables forces exceeding 1 N and displacements approaching 1 mm with response

M. Linnander, and Y. Visell are with the Department of Mechanical Engineering, University of California, Santa Barbara, 93106 USA (e-mail: maxlinnander@ucsb.edu; yonvisell@ucsb.edu).

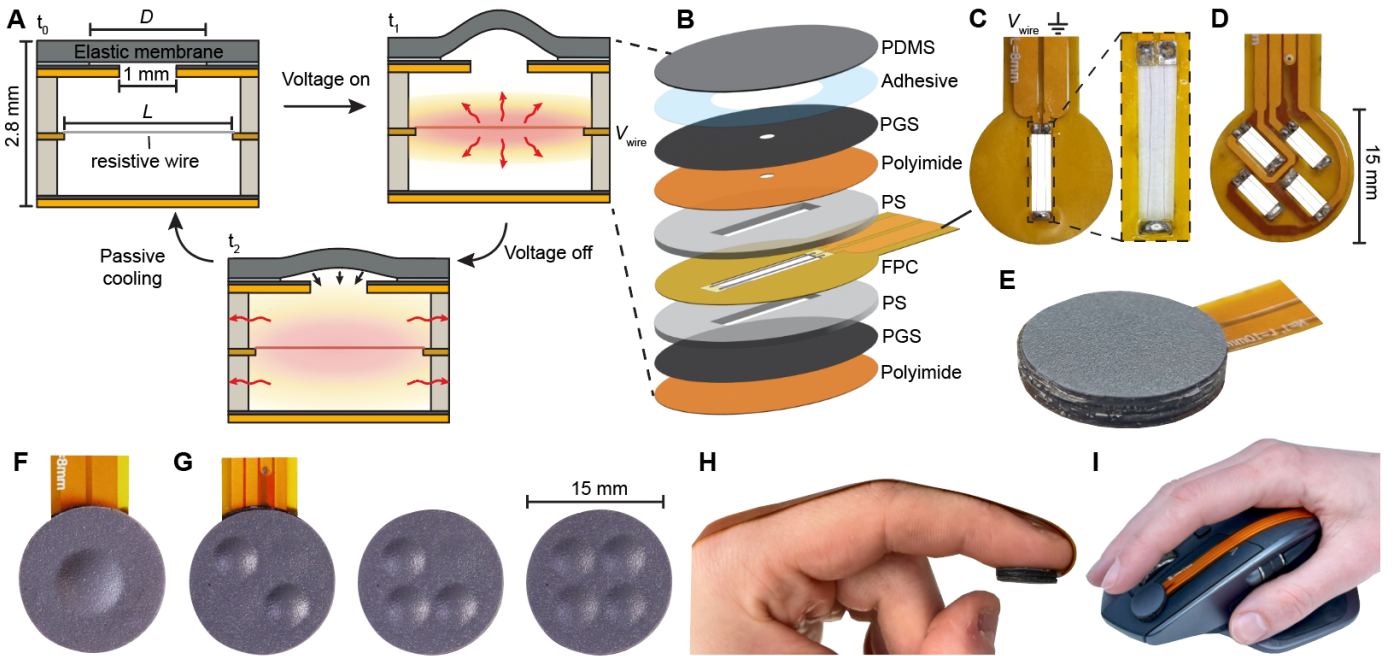


Fig. 1. A) Operating principle for thermopneumatic pixels (TPPs). TPPs deliver heat to air encapsulated within a small sealed cavity, driving gas expansion that yields localized forces and displacements. Heat is supplied to the gas (air) via transient Joule heating of a resistive Nickel-Chromium (NiCr) wire suspended in the cavity. Due to the small diameter of the wire (48 AWG), heat is rapidly transferred to the gas, driving a rapid pressure increase in the gas. The air pressure increase drives deflection of an elastic membrane sealing the top of the cavity, yielding localized forces and displacements. B) The design uses a simple, layered assembly of common materials. Exploded view of the multilayer TPP stack, comprising patterned structural, thermal, and compliant layers. C) Photograph of flexible printed circuit (FPC) layers with suspended NiCr wires, for a module with a single small TPP (cavity length $L = 8$ mm). The dashed box shows an enlarged view of the NiCr wire. D) FPC layer for a quartet module with four TPPs ($L = 4$ mm). E) Photograph of the module. F) Top-down view of TPP during actuation ($L = 8$ mm, pixel diameter $D = 6$ mm) G) Top-down view of the quartet module, with four TPPs, as it displays different patterns ($L = 4$ mm, $D = 4$ mm). H-I) Examples of how TPPs can be integrated into common interaction forms.

times on the order of 5–100 ms, satisfying key requirements for high-fidelity tactile stimulation. The simple, layer-based construction and use of inexpensive, readily available materials facilitate rapid fabrication and scalable integration into spatially distributed systems. We further present driving electronics capable of operating multiple modules concurrently, illustrating the modularity and ease of deployment of the system. Finally, we characterize the mechanical, dynamic, and thermal behavior of the TPPs and report perceptual results demonstrating robust, perceivable tactile feedback across a broad range of drive conditions.

II. DESIGN AND OPERATING PRINCIPLE

TPPs deliver fast, localized tactile feedback by heating air encapsulated in small volumes (6 to 32 μL) in order to drive rapid pressure increases that deflect a top membrane, forming the pixel’s touch surface. Their fast responses are facilitated by a favorable physical scaling regime, notably the high rate of heat transfer that is achievable at small dimensions, and the low thermal mass of air.

Each TPP operates on an electro-thermo-mechanical principle, in which electrical energy is converted into heat within a thin resistive wire when a voltage, V_{wire} , is applied across it (Fig. 1A). Owing to the low thermal mass of the wire, its temperature rises rapidly, producing a transient increase in the temperature and pressure of the enclosed gas. The resulting gas expansion deflects an elastic membrane, generating dynamic

forces $F(t)$ and displacements $z(t)$. Following termination of the electrical pulse, heat dissipates to the surrounding structure and environment, allowing the TPP to return to its initial state.

This actuation strategy admits many possible implementations; here we describe one realization. To support scalable fabrication and ease of integration, we employed a simple, layered architecture (Fig. 1B). Joule heating is supplied via an active layer, comprising a flexible printed circuit (FPC, 120 μm thick) with a rectangular cutout of length L and width w . For the TPPs demonstrated here, L ranges from 2 to 10 mm, and is held constant at $w = 2$ mm. Two fine, 48 AWG Nickel-Chromium (NiCr) wires are suspended along the length of the cutout (Fig. 1C). The wires are electrically connected at one end of the cavity to form a continuous resistive heating element.

On both sides of the FPC are vinyl-cut and laser-cut layers of polyimide (125 μm), pyrolytic graphite sheet (PGS, 17 μm), polysiloxane (PS, 0.8 mm), adhesive, and a compliant polydimethylsiloxane (PDMS) membrane (250 μm) that functions as the tactile surface. The PS layer contains a matching $L \times w$ mm cutout aligned with the FPC cavity. Circular apertures in the overlying polyimide and PGS layers create a central opening that permits pressurization of the cavity to deflect the PDMS membrane. The effective pixel diameter D is set by a circular cutout in the adhesive layer beneath the PDMS (Fig. 1A). A full list of materials can be found in Appendix A.

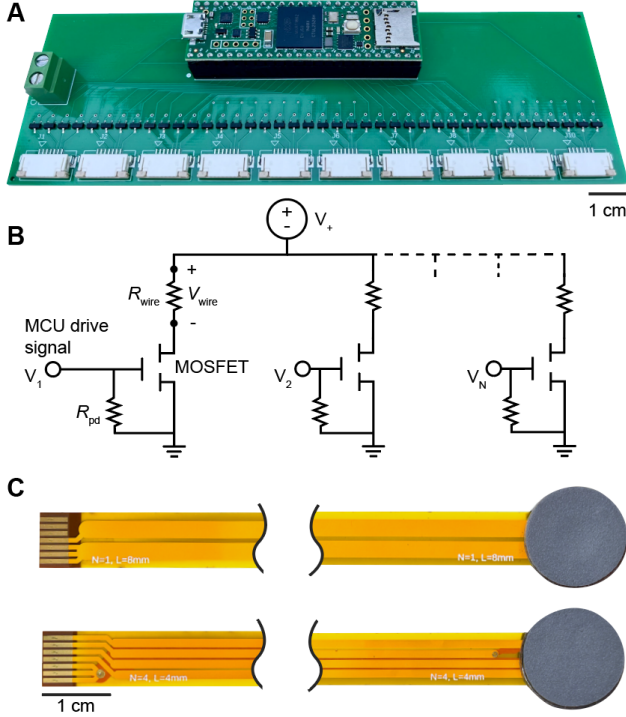


Fig. 2. A) Electronic driver board interfacing with up to ten modules, enabling simultaneous operation of up to forty TPPs in the quartet configuration. B) General schematic used to drive the TPPs. C) The single and quartet modules share a common electrical pinout to facilitate operation with the driver board. The photos show modules with a single TPP (top, $L = 8$ mm) and quartet (bottom, $L = 4$ mm). The connector length is application-dependent.

We use NiCr as the heating element due to its thermal stability and resistance to oxidation at elevated temperatures, and incorporate pyrolytic graphite sheets (PGS) to provide high in-plane thermal conductivity for passive lateral heat spreading. To support rapid prototyping and straightforward integration into interactive systems, we implement modules as slim, mechanically flexible circular pads (15 mm diameter, 2.8 mm thick) that can be mounted on curved or planar surfaces and configured with one or multiple TPPs (Fig. 1E–I).

To demonstrate the ease with which these modules can be driven, we designed an electrical driver board (Fig. 2). We implemented a common electrical pinout for driving both configurations shown in (Fig. 1F–G) – the quartet of four smaller TPPs and the single TPP. The electronic driver board is capable of operating up to ten such modules, enabling simultaneous operation of up to forty TPPs in the quartet configuration or ten in the single TPP configuration shown. The modules connect to the driver board via zero-insertion-force connectors (Fig. 2C). Each TPP is driven by brief, voltage-controlled electrical pulses (0.5–100 ms) supplied by an external programmable power supply and gated by a MOSFET switch. Pulse timing is generated directly on the microcontroller unit (MCU), which interfaces with a host computer and delivers gate-drive signals to the MOSFETs. Each gate is connected to a pull-down resistor, R_{pd} , to prevent floating when inactive (Fig. 2B). Additional system-level details are provided in Appendix A.

III. ACTUATOR CHARACTERIZATION

A. Thermomechanical Characterization

We characterized the thermal and mechanical responses of the actuator under electrical pulse excitation with duration t_p and voltage V_{wire} (Fig. 3). The force output at the tactile membrane, $F(t)$, was measured isometrically, using a load cell (Futek LSB200). Free (unloaded) displacement was measured using a laser triangulation sensor (Keyence IL-065). The cavity air temperature, $T_{air}(t)$, was computed as follows. From the measured force $F(t)$, we computed the gauge air pressure $P(t) = F(t)/A$, where $A = \pi(D/2)^2$ is the pixel area, where D is the membrane aperture diameter. Air temperature was obtained using the ideal gas law, $T_{air}(t) = T_0(F(t)/(P_0 A) + 1)$, where P_0 and T_0 are the initial cavity pressure and temperature. The temperature of the NiCr heating element, $T_{wire}(t)$, was computed from in situ resistivity measurements using a resistivity–temperature relationship (Appendix B).

We observed the temperature of the NiCr wire, $T_{wire}(t)$, to increase monotonically upon application of a voltage, driving corresponding increases in cavity air temperature and pressure. The resulting membrane force, $F(t)$, produced a displacement, $z(t)$ (Fig. 3A). Temperature, pressure, force, and displacement exhibited closely matched temporal profiles and reached peak values near the end of the applied pulse. Over the timescales examined, these variables were strongly correlated and appeared primarily related through approximately constant gain factors, rather than distinct dynamics, consistent with prior observations in thermopneumatic actuators of similar dimensions [19], [20].

Heat transfer from the suspended wire to the surrounding air and structure can be approximated using a first-order lumped thermal model, yielding a wire temperature response of the form

$$T_{wire}(t) = P_{el} R_{thermal} (1 - e^{-t/\tau}), \quad (1)$$

where $P_{el} = V_{wire}^2/R_{wire}$ is the electrical power dissipated in the NiCr wire, with V_{wire} and R_{wire} being the voltage and resistance across the wire. The effective thermal resistance, $R_{thermal}$, accounts for heat transfer through the air and wire, while the characteristic time constant $\tau = R_{thermal}C$, governs the heating and cooling dynamics, where C is the heat capacity of the wire.

For a TPP with $L = 8$ mm, $D = 6$ mm, electrical power of $P_{el} = 4.8$ W and a pulse duration of $t_p = 75$ ms, the wire temperature reached a peak value of $T_{wire} = 1090$ °C, corresponding to an inferred air temperature of 97 °C, a peak membrane force of 750 mN, and a free displacement of 0.96 mm. Following termination of the pulse, the system returned toward its initial state with a time constant of $\tau = 110$ ms, obtained by fitting Eq. 1 to the cooling transient ($r^2 = 0.98$). Consistent with Eq. 1, the peak force increased monotonically with both pulse duration and electrical power (Fig. 3B–C).

To enable a comparison across geometries, we parameterized the power level by the electrical power dissipated per unit wire length, $\rho = P_{el}/L_T$. Here, $L_T = 2L + 1$ is the total wire length, accounting for routing across the cavity and

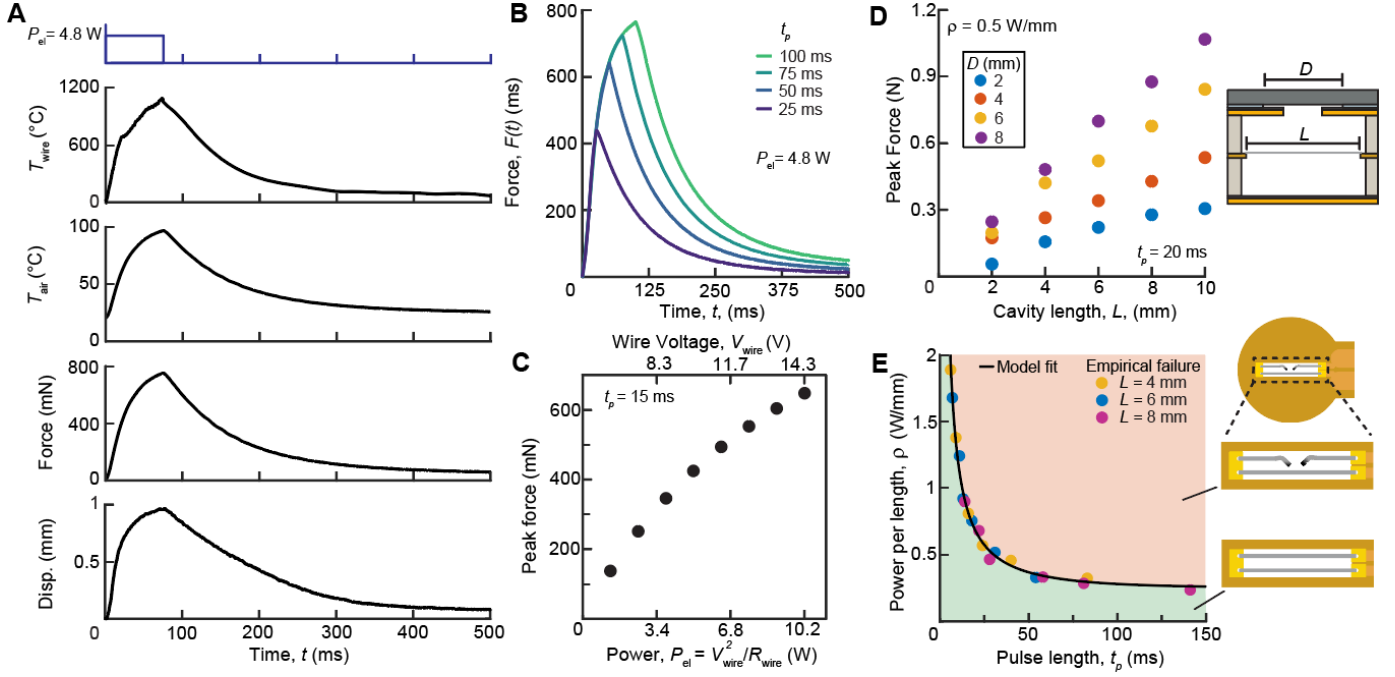


Fig. 3. Thermomechanical characterization of TPPs. A) NiCr wire temperature $T_{\text{wire}}(t)$, inferred cavity air temperature $T_{\text{air}}(t)$, isometric force $F(t)$, and free displacement $z(t)$ in response to a 75-ms, 4.8 W electrical pulse. B) Force response $F(t)$ for increasing pulse durations t_p at fixed electrical power. C) Peak force as a function of electrical power dissipated in the wire, $P_{\text{el}} = V_{\text{wire}}^2/R_{\text{wire}}$, for $t_p = 15$ ms. D) Peak force measured across actuators with varying cavity length L and aperture diameter D , at fixed power per unit length $\rho = 0.5$ W/mm. E) Operating envelope of TPPs, defined by power per unit length ρ and pulse duration t_p . Shaded regions indicate viable operation (green) and empirical failure (red). Points denote measured failure events for varying L , and the black curve shows a fit to an analytic thermal model.

back to the solder holes. In practice, the pair (ρ, t_p) largely determines the peak wire temperature, and therefore provides a geometry-agnostic parameterization of the actuator’s viable operating regime.

Using this parametrization, we examined how actuator geometry influences peak force output when driven at a power per unit length of $\rho = 0.5$ W/mm. Across TPPs with varying cavity length L and membrane aperture diameter D , peak force increased monotonically with both parameters and reached a maximum measured value of 1.07 N (Fig. 3D).

We next sought to identify the usable driving regime of the actuators. Owing to the low thermal mass of the NiCr wire, excessive drive conditions can rapidly result in wire melting and actuator failure. Specifically, we drove actuators with $L = 4, 6,$ and 8 mm to failure over a range of pulse durations t_p and power per unit length values ρ (Fig. 3E). For each actuator, we identified the minimum pulse duration t_p that caused wire failure, which occurred via melting near $T_{\text{wire}} = 1400$ °C [21]. Across lengths L and driving levels ρ , the identified failure boundary clearly circumscribes the usable operating envelope of the TPPs (Fig. 3E, shaded green area) – a constraint surface that we parametrically fit to the observed data (see Appendix C for details).

B. Characterization During Cyclic Stimulation

During interactions with everyday objects, the human hand is exposed to tactile stimuli spanning a wide range of temporal frequencies. In particular, the skin is sensitive to transient displacements on timescales of approximately 1–10 ms [22],

making the dynamic response of a tactile actuator a critical performance consideration. As shown in Fig. 4, the TPPs support cyclic operation over a wide range of pulse rates, with pulse durations between 5 and 100 ms, despite a longer thermal relaxation time of $\tau = 110$ ms. Under such cyclic excitation, the force response can be decomposed into a slowly varying offset component, F_0 , arising from residual heat accumulation in the cavity, and a pulse-synchronous component, F_{pp} , that tracks the applied pulse rate [18]–[20]. This separation aligns well with tactile perception, which is known to be more sensitive to transient, high-frequency components of mechanical stimulation than to low-frequency or quasi-static inputs [22].

Given the heightened sensitivity of the tactile system to transient, high-frequency components of mechanical stimulation, the peak-to-peak force component, F_{pp} , is the primary metric of interest. We measured F_{pp} for pulse rates f between 10 and 200 Hz (Fig. 4B), over which F_{pp} ranged from 332 mN to 7.0 mN. Across this interval, the peak-to-peak force exhibited an approximately inverse dependence on frequency, with a slope near -1 in log–log space. This scaling is consistent with the fact that, for fixed electrical power P_{el} and duty cycle $t_p/\Delta t$ (where Δt is the pulse period), the energy delivered per pulse decreases with increasing pulse rate, $E \propto 1/f$. Inset magnitude spectra (high-pass filtered) show strong spectral peaks at the drive frequency and its harmonics, consistent with the sawtooth-like temporal force waveform (insets in Fig. 4B).

We evaluated the reliability of the actuator over 54,000 actuation cycles and observed no meaningful degradation

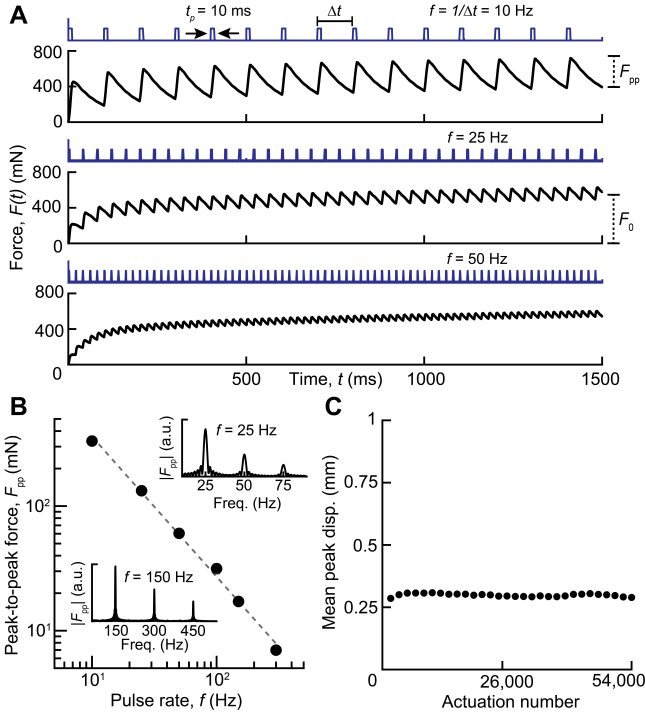


Fig. 4. Characterization of TPPs under cyclic operation. A) Isometric force responses to pulse trains at pulse rates $f = 10, 25,$ and 50 Hz (top to bottom) at duty cycle $t_p/\Delta t = 0.1$. B) Peak-to-peak force component F_{pp} as a function of pulse rate f with duty cycle $t_p/\Delta t = 0.1$. Regression fit: $\log_{10}(F_{pp}) = \alpha \log_{10}(f) + \beta$, $\alpha = -1.12$, $\beta = 3.68$, $r^2 > 0.99$. Insets show the magnitude spectra of the measured force signals for pulse rates of 25 and 150 Hz. (c) Mean free displacement is consistent over 54,000 actuations. Each dot corresponds to the mean of 90 peaks.

in dynamic performance (Fig. 4C). The driving parameters used, $\rho = 0.42$ W/mm and $t_p = 19$ ms, correspond to an inferred peak wire temperature of approximately 800 °C and air temperature of 80 °C, reached during each pulse. At this temperature, NiCr exhibits strong resistance to oxidation, supporting stable operation under extended cyclic actuation [23].

C. Surface Temperature Characterization

We measured the maximum surface temperature increase, ΔT_{surf} , at the center of the membrane, and found that surface heating remained low for the conditions examined (Fig. 5). Across all conditions tested, the maximum membrane temperature rise was $\Delta T_{\text{surf}} = 4.6$ °C, comparable to the temperature increase induced by a finger in contact with the surface [19]. Measurements were performed during continuous pulsed operation over a 5-s window with duty cycle $t_p/\Delta t = 0.2$ and pulse rate $f = 20$ Hz, while varying cavity length L and power per unit length ρ . With duty cycle held constant, ΔT_{surf} varied little across geometries and was mainly influenced by ρ . To place these measurements in context, tactile actuators are rarely driven continuously at high power for more than brief intervals, as sustained stimulation can be uncomfortable and subject to sensory adaptation [24]. Consistent with this, modern consumer devices typically employ short vibrational bursts rather than prolonged actuation.

IV. PERCEPTUAL EXPERIMENTS

We conducted two perceptual experiments to evaluate tactile feedback delivered by the thermopneumatic pixels (TPPs). The first study characterized perceived intensity as a function of power, P_{el} . The second study consisted of a localization task where the user identified which TPP on their finger pad was active.

We recruited ten people who volunteered to participate without compensation (4 female; finger pad width 1.3 to 1.9 cm; ages 20 to 29). All participants provided their written informed consent, and the experimental protocol was approved by the human subjects review board at the authors' institution (protocol number: 13-22-0139). At the start of each experiment, before data collection, participants experienced several stimuli and practiced entering responses for familiarization. No feedback about responses was supplied to participants during this phase, and the data were not used for analysis.

In the first experiment, we assessed perceived tactile intensity I as a function of dissipated electrical power P_{el} , finding that perceived intensity, $I(P_{\text{el}})$, increased linearly with power (Fig. 6A). The experiment used the psychophysical method of magnitude estimation [25], [26]. This experiment used the TPP module with a single pixel ($L = 10$ mm and $D = 8$ mm; Fig. 1G). The stimuli were pulse trains ($f = 20$ Hz, $t_p/\Delta t = 0.2$, duration = 0.5 s) at each of 5 different power levels ($P_{\text{el}} = 1.2$ to 6 W). Each stimulus was presented 7 times. Participants rated the intensity of each stimulus on a continuous numerical scale on a computer interface. The extremes of the scale were labeled “no sensation” and “strongest imaginable”. Perceived intensity, $I(P_{\text{el}})$, was computed for each power level P_{el} by averaging the normalized geometric mean of responses across all participants [25]. Using these results, a desired intensity level can be generated by driving the TPP with the corresponding power. In experiment 2, participants reported which single TPP was actuated out of four TPPs ($L = 4$ mm, $D = 4$ mm) arranged in a grid under their finger pad (Fig. 6B). They responded correctly on 95.5% of trials. The stimuli were pulse trains ($f = 20$ Hz, $t_p/\Delta t = 0.2$, duration = 0.5 s, $P_{\text{el}} = 2.8$ W) with 28 trials per participant (4 locations x 7 repetitions). In post-experiment surveys, nine participants reported feeling no warmth from

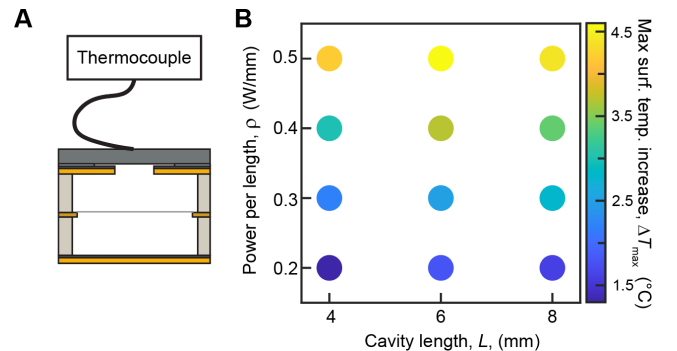


Fig. 5. A) Surface temperature measurements of TPPs. (b) Max temperatures measured during a 5-s actuation window for varying L and ρ at a duty cycle of $t_p/\Delta t = 0.2$.

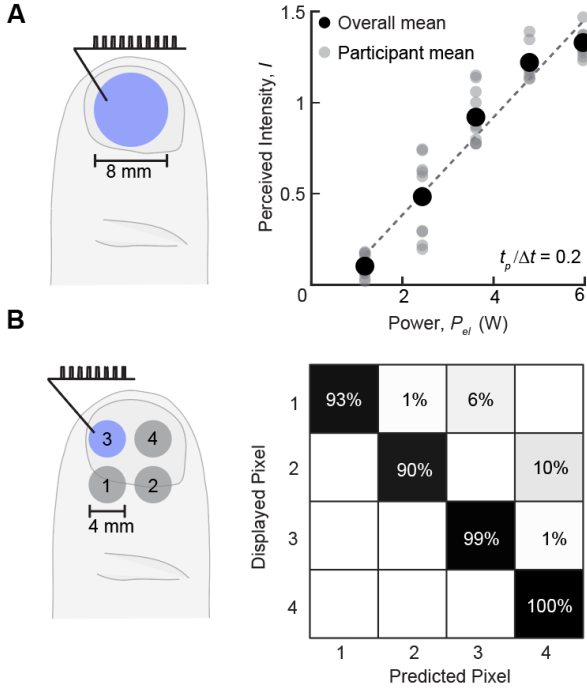


Fig. 6. Perceptual Evaluation. A) Experiment 1: Perceived intensity as a function of power, measured using the method of magnitude scaling. Regression fit: $I = \alpha P_{el} + \beta$, $\alpha = 0.2677$, $\beta = -0.151$, $r^2 = 0.97$. B) Experiment 2: Spatial localization of active TPP on the finger pad.

the TPP modules, while one participant reported feeling slight warmth.

V. CONCLUSION

In conclusion, we presented low-voltage thermopneumatic pixels (TPPs) and flexible arrays that deliver localized tactile feedback in compact form factors. Each actuator operates at ~ 10 V with millisecond-scale response and produces displacements approaching 1 mm and forces exceeding 1 N. We also introduced a driving system capable of concurrently operating up to ten modules (forty TPPs) and showed, through perceptual evaluation, that the resulting cues are salient and reliably perceived. Together, these results underscore thermopneumatic actuation as a practical approach for embedding tactile feedback into experimental prototypes and emerging interactive devices.

APPENDIX A HARDWARE COMPONENTS FOR TACTILE DISPLAY

TABLE I
ELECTRICAL COMPONENTS USED IN THE CUSTOM DRIVING CIRCUIT FOR CONTROLLING UP TO 40 TPPS.

Component	Part Number	Quantity	Cost
Microcontroller	Teensy 4.1	1	\$33.6
MOSFET	AO3400A	40	\$1.97
Resistor	0402WGF3302TCE	40	\$0.03
Connector	691137710002	1	\$0.7
Connector	522070760	10	\$2.79
Connector	PPPC241LFBN-RC	2	\$4.4
Total Cost			\$43.49

TABLE II
COMPONENTS USED FOR ONE TPP MODULE

Component	Part Number	Unit Cost
FPC	JLPCB Custom Design	\$2.2
NiCr Wire	Wire Optim 354-23	\$0.01
Polyimide	McMaster-Carr 2271K73	\$0.24
Polysiloxane	McMaster-Carr 86915K24	\$0.24
Adhesive	3M 2477	\$0.01
PDMS	McMaster-Carr 86435K41	\$0.12
PGS	HPMS Graphite HGS-012-12A	\$0.2
Total Cost		\$3.02

APPENDIX B

WIRE TEMPERATURE FROM RESISTANCE MEASUREMENT

The wire temperature, $T_{\text{wire}}(t)$, in Fig. 3A was computed from resistance measurements of the NiCr wire during actuation. A shunt resistor ($R_{\text{shunt}} = 0.22 \Omega$) was placed in series with the TPP, and the voltage drop across it, $V_{\text{shunt}}(t)$, was measured during actuation. Assuming that the driving voltage V_+ was constant, and that there was a negligible temperature rise in the shunt and remaining circuitry ($R_{\text{circuit}} = 2.1 \Omega$), we obtained the total series resistance via the inverse voltage divider relation,

$$R_{\text{tot}}(t) = \frac{V_+ R_{\text{shunt}}}{V_{\text{shunt}}(t)}.$$

The instantaneous wire resistance was then calculated as $R_{\text{wire}}(t) = R_{\text{tot}}(t) - R_{\text{shunt}} - R_{\text{circuit}}$. The relative resistivity change was referenced to the initial wire resistance, and the corresponding temperature rise was estimated by linearly interpolating tabulated resistivity–temperature data for NiCr [21]. The resulting temperature trace was smoothed using a moving-average filter and downsampled for visualization.

APPENDIX C

OPERATING ENVELOPE FIT

The experimentally observed operating envelope boundary in Fig. 3E was fit using the lumped-parameter thermal model for the NiCr heating element (Eq. 1). Solving Eq. 1 for P_{el} and normalizing by the total wire length L_T yields the power per unit length, $\rho = P_{el}/L_T$, in terms of pulse duration t_p ,

$$\rho(t_p) = \frac{T_{\text{fail}}}{a(1 - e^{-t_p/b})} \quad (2)$$

Here, the wire failure temperature, $T_{\text{fail}} = 1400$ °C, was set to the melting temperature of NiCr. The fitting parameters a and b capture the length-scaled thermal properties of the heating element, with $a = R_{\text{thermal}} L_T$ representing the thermal resistance and $b = C/L_T$ the thermal mass. The analytic fit closely aligned with the measured failure points ($a = 6601$ mm K/W, $b = 6.51 \mu\text{J}/\text{mm K}$, $r^2 = 0.99$), delineating a region of stable operation (green) from drive conditions that lead to failure (red) (Fig. 3E).

REFERENCES

- [1] D. Goetz, G. Reardon, M. Linnander, and Y. Visell, “Dynamic feedback in wave-mediated surface haptics: A modular platform,” in *2023 IEEE World Haptics Conference (WHC)*. IEEE, 2023, pp. 107–113.

- [2] N. Tummala, G. Reardon, S. Fani, D. Goetz, M. Bianchi, and Y. Visell, "Skinsource: A data-driven toolbox for predicting touch-elicited vibrations in the upper limb," in *2024 IEEE Haptics Symposium (HAPTICS)*, 2024, pp. 53–60.
- [3] B. Huang, S. Ren, Y. Luo, Q. Cheng, H. Cai, Y. Sang, M. Sousa, P. H. Dietz, and D. Wigdor, "Vibraforge: A scalable prototyping toolkit for creating spatialized vibrotactile feedback systems," in *Proceedings of the 2025 CHI Conference on Human Factors in Computing Systems*, ser. CHI '25. New York, NY, USA: Association for Computing Machinery, 2025.
- [4] N. Rokhmanova, J. Martus, R. Faulkner, J. Fiene, and K. J. Kuchenbecker, "Open-source hardware and software platform for vibrotactile motion guidance," *Device*, p. 100966, Oct. 2025.
- [5] L. Jones and S. Lederman, *Human hand function*. Oxford University Press, 2006.
- [6] D. Copeland and J. Finlay, "Identification of the optimum resolution specification for a haptic graphic display," *Interacting with Computers*, vol. 22, no. 2, pp. 98–106, 2010.
- [7] J. C. Craig and P. M. Evans, "Vibrotactile masking and the persistence of tactual features," *Perception and psychophysics*, vol. 42, no. 4, pp. 309–317, 1987.
- [8] J. Streque, A. Talbi, P. Pernod, and V. Preobrazhensky, "Pulse-driven magnetostatic micro-actuator array based on ultrasoft elastomeric membranes for active surface applications," *Journal of Micromechanics and Microengineering*, vol. 22, no. 9, p. 095020, aug 2012.
- [9] E. Leroy and H. Shea, "Hydraulically amplified electrostatic taxels (haxels) for full body haptics," *Advanced Materials Technologies*, vol. 8, no. 16, p. 2300242, 2023.
- [10] G. Grasso, S. Rosset, and H. Shea, "Fully 3d-printed, stretchable, and conformable haptic interfaces," *Advanced Functional Materials*, vol. 33, no. 20, p. 2213821, 2023.
- [11] S. K. Mitchell, T. Martin, and C. Keplinger, "A pocket-sized ten-channel high voltage power supply for soft electrostatic actuators," *Advanced Materials Technologies*, vol. 7, no. 8, p. 2101469, 2022. [Online]. Available: <https://advanced.onlinelibrary.wiley.com/doi/abs/10.1002/admt.202101469>
- [12] S. Biswas and Y. Visell, "Emerging material technologies for haptics," *Advanced Materials Technologies*, vol. 4, no. 4, p. 1900042, 2019.
- [13] C. Shultz and C. Harrison, "Flat panel haptics: Embedded electroosmotic pumps for scalable shape displays," in *Proceedings of the 2023 CHI Conference on Human Factors in Computing Systems*, ser. CHI '23. New York, NY, USA: Association for Computing Machinery, 2023.
- [14] V. Shen, T. Rae-Grant, J. Mullenbach, C. Harrison, and C. Shultz, "Fluid reality: High-resolution, untethered haptic gloves using electroosmotic pump arrays," in *Proceedings of the 36th Annual ACM Symposium on User Interface Software and Technology*, ser. UIST '23. New York, NY, USA: Association for Computing Machinery, 2023.
- [15] C. J. Camargo, H. Campanella, J. E. Marshall, N. Torras, K. Zinoviev, E. M. Terentjev, and J. Esteve, "Batch fabrication of optical actuators using nanotube–elastomer composites towards refreshable braille displays," *Journal of Micromechanics and Microengineering*, vol. 22, no. 7, p. 075009, jun 2012. [Online]. Available: <https://dx.doi.org/10.1088/0960-1317/22/7/075009>
- [16] T. Hiraki, K. Nakahara, K. Narumi, R. Niiyama, N. Kida, N. Takamura, H. Okamoto, and Y. Kawahara, "Laser pouch motors: Selective and wireless activation of soft actuators by laser-powered liquid-to-gas phase change," *IEEE Robotics and Automation Letters*, vol. 5, no. 3, pp. 4180–4187, 2020.
- [17] A. Mazzotta and V. Mattoli, "Ultrathin conformable electronic tattoo for tactile sensations," *Advanced Electronic Materials*, vol. 9, no. 9, p. 2201327, 2023.
- [18] A. Mazzotta, S. Taccola, I. Cesini *et al.*, "Low-voltage wearable tactile display with thermo-pneumatic actuation," *npj Flexible Electronics*, vol. 9, no. 70, 2025. [Online]. Available: <https://doi.org/10.1038/s41528-025-00426-3>
- [19] M. Linnander, D. Goetz, G. Reardon, V. Kumar, E. Hawkes, and Y. Visell, "Tactile displays driven by projected light," *Science Robotics*, vol. 10, no. 107, p. eadv1383, 2025. [Online]. Available: <https://www.science.org/doi/abs/10.1126/scirobotics.adv1383>
- [20] M. Linnander and Y. Visell, "Haptic light-emitting diodes: Miniature, luminous tactile actuators," *arXiv preprint arXiv:2601.11043*, 2026. [Online]. Available: <https://arxiv.org/abs/2601.11043>
- [21] Alloy Wire International Ltd., "80/20 ni cr resistance wire: Technical datasheet aws 180 rev.1," Alloy Wire International Ltd., Brierley Hill, West Midlands, UK, Technical Datasheet AWS 180 Rev.1, 2016, available at: <https://www.alloywire.com>.
- [22] M. Morioka and M. J. Griffin, "Thresholds for the perception of hand-transmitted vibration: dependence on contact area and contact location," *Somatosensory and Motor Research*, vol. 22, no. 4, pp. 281–297, 2005.
- [23] J. Zhou, T. R. Ohno, and C. A. Wolden, "High-temperature stability of nichrome in reactive environments," *Journal of Vacuum Science and Technology A*, vol. 21, no. 3, pp. 756–761, 04 2003. [Online]. Available: <https://doi.org/10.1116/1.1570834>
- [24] R. T. Verrillo and G. A. Gescheider, "Effect of prior stimulation on vibrotactile thresholds," *Sensory Processes*, vol. 1, no. 4, pp. 292–300, 1977.
- [25] L. A. Jones and H. Z. Tan, "Application of psychophysical techniques to haptic research," *IEEE Transactions on Haptics*, vol. 6, no. 3, pp. 268–284, 2013.
- [26] S. S. Stevens, "Problems and methods of psychophysics," *Psychological bulletin*, vol. 55, no. 4, p. 177, 1958.